Supporting Information
©Wiley-VCH 2021
69451 Weinheim, Germany

Digital and Tunable Genetically Encoded Tension Sensors Based on Engineered Coiled-Coils

Shuhong Liu, Jinchan Liu, Alexander Foote, Hiroaki Ogasawara, Sarah Al Abdullatif, Victor S. Batista, and Khalid Salaita*

Abstract: Genetically encoded tension sensors (GETSs) allow for quantifying forces experienced by intracellular proteins involved in mechanotransduction. The vast majority of GETSs are comprised of a FRET pair flanking an elastic "spring-like" domain that gradually extends in response to force. Because of ensemble averaging, the FRET signal generated by such analog sensors conceals forces that deviate from the average, and hence it is unknown if a subset of proteins experience greater magnitudes of force. We address this problem by developing digital GETSs comprised of coiled-coils (CCs) with tunable mechanical thresholds. We validate the mechanical response of CC digital probes using thermodynamic stability prediction, AlphaFold2 modeling, steered molecular dynamics simulations, and single molecule force microscopy. Live cell measurements using optimized CC tension sensors that are inserted into vinculin demonstrate that 13% of this mechanosensor experiences forces > 9.9 pN within focal adhesions. This reveals greater magnitudes of vinculin force than had previously been reported and demonstrates that coiled-coil tension sensors enable more facile and precise tension measurements in living systems.

Table of Contents

S1. Methods and materials

1.1 Generation of tension sensor and force insensitive constructs.

To create the first TS-CC, TS-(S_0N-), GGSGGS7 linker in tCRMod-GGSGGS7 (Addgene plasmid # 111761)[1] was replaced by CC-S_0N- domain (AQL EKE LQA LEK ENA QLE WEL QAL EKE LAQ GGS GGS AQL KKK LQA LKK KNA QLK WKL QAL KKK LAQ) overhung by 5′BspEI/3′AgeI. The backbone of TS-(S_0N-) was digested from tCRMod-GGSGGS7 using restriction enzyme KpnI and BsrGI (NEB). The DNA sequence from restriction sites KpnI to BsrGI on TS-(S_0N-) was synthesized (5′-CGA CGG TAC CTA CAA GAC CCG CGC CGA GGT GAA GTT CGA GGG CGA CAC CCT GGT GAA CCG CAT CGA GCT GAA GGG CAT CGA CTT CAA GGA GGA CGG CAA CAT CCT GGG GCA CAA GCT GGA GTA CAA CTT CAA CAG CCA CAA CGT CTA TAT CAC GGC CGA CAA GCA GAA GAA CGG CAT CAA GGC TAA CTT CAA GAT CCG CCA CAA CGT TGA GGA CGG CAG CGT GCA GCT CGC CGA CCA CTA CCA GCA GAA CAC CCC CAT CGG CGA CGG CCC CGT GCT GCT GCC CGA CAA CCA CTA CCT GAG CCA TCA GTC CGC CCT GAG CAA AGA CCC CAA CGA GAA GCG CGA TCA CAT GGT CCT GCT GGA GTT CGT GAC CGC CGC CGG GTC CGG AGC TCA GTT GGA GAA AGA ACT GCA GGC TCT TGA AGA GAA TGC TCA GTT GGA ATG GGA GCT TCA GGC ACT GGA GAA GGA GCT GGC TCA AGG CGG TTC AGG GGG CAG CGC CCA ACT CAA AAA GAA ATT GCA AGC ATT GAA AAA AAA AAA TGC CCA ACT TAA GTG GAA ACT GCA GGC CCT TAA GAA GAA ACT CGC CCA GAC CGG TAA GGG CGA AGA GCT GAT CAA GGA AAA TAT GCG TAT GAA GGT GGT CAT GGA AGG TTC GGT CAA CGG CCA CCA TTC AAA TGC ACA GGT GAG GAG AGG CAA TCC GTA CAT GGG AAC TCA AAC CAT GAG GAT CAA AGT CAT CGA GGG AGG ACC CCT GCC ATT GCT TCT TGA CAT TCT TGC CAC GTC GTT CAT GTA TGG CAG CCG TAC TTT TAT CAA GTA CCC GAA AGG CAT CCC TGA TTT CTT TAA ACA GTC CTT CCC TGA GGG TTT TAC TTG GGA AAG AGT TAC GAG ATA CGA AGA TGG TGG AGT CGT CAC CGT CAT GCA GGA CAC CAG CCT TGA GGA TGG CTG TCT CGT TTA CCA CGT CCA AGT CAG AGG GGT AAA CTT CCC TCA AGG TCC CGT GAT GCA GAA GAA GAC CAA GGG TTG GGA GCC TAA TAC AGA GAT GAT GTA TCC AGC AGA TGG TGG TCT GAG GGG ATA CAC TCA TAT GGC ACT GAA AGT TGA TGG TGG TGG CCA TCT GTC TTG CTC TTT CGT AAC AAC TTA CAG GTC AAA AAA GAC CGT CGG GAA CAT CAA GAT GCC CGG TAT CCA TGC CGT TGA TCA CCG CCT GGA AAG GTT AGA GGA AGG TGA CAA TGA AAT GTT CGT AGT ACA ACG CGA ACA CGC AGT TGC AAG TTC GCC GGG CTG GTG GTG GGA TGG ACG ACT GTA CAA GGC-3′; Twist Bioscience) and inserted to the digested backbone by standard DNA ligation. For force insensitive control Fi-(S_0N-), Clover-(CC-S_0N-)-mRuby2 domain was attached at the end of vinculin with 5′EcoRI/3′XbaI overhang, after digesting Vinculin-Venus (Addgene plasmid # 27300)[2] with restriction enzyme EcoRI and XbaI (NEB). For mutations of tension sensor constructs (TSs) and force insensitive constructs (Fis), CC-domain CC-S_0N- was replaced with CC-S_0, CC-S_2, CC-S_4, CC-S_7, CC-S_1, CC-M_2, and CC-M_{ad}, respectively. DNA sequence with 5′BspEI/3′BsrGI was synthesized from Twist Bioscience. Next, TS-S_0N- and Fi-S_0N- was digested with restriction enzymes BspEI and BsrGI, then ligated with synthesized mutated inserts. Condensate control plasmid constructs were generated based on TS-S_0 with CC linkers-mRuby3 replaced by GCN4. The DNA with 5′BspEI/3′BsrGI overhang was synthesized and inserted to TS-S_0 digested using BspEI and BsrGI. All sequences were confirmed by sanger sequencing (Azenta) with the primer 5′-CCC CGT GCT GCT GCC CGA CAA CCA-3′.

1.2 Generation of His-AviTag-CC expression constructs.

For single-molecule force spectroscopy calibration, C-terminal cysteine was added to CCs to allow attachment of the DNA handle. N-terminal HisTag was added for purification and AviTag, for biotinylation. DNA sequence containing CC domain was synthesized (5′-CAG CCA TAT GGG TCT GAA TGA TAT TTT CGA AGC GCA GAA AAT TGA ATG GCA TGA AGG TAG CGG AGG TGG TTC AGC CCA ATT AGA AAA GGA GCT GCA GGC ACT TGA AGA GAA TGC TCA GTT AGA GTG GGA ACT TCA AGC ATT GGA GAA GGA ACT GGC ACA GGG CGG TAG TGG CGG CAG CCA AGC GTT GAA AAA GAA ACT GGC GCA GCT GAA ATG GAA GTT GCA GGC CAA TAA AAA GAA GCT GGC TCA ACT GAA GAA AAA GTT GCA GCC GGG GGA GCT CGA GCT GTT AAA GCT TGC GG-3′; Twist Bioscience) including a 5′NdeI/3′HindIII overhang, was then inserted to AviTag-SpyTag003-MBP (Addgene Plasmid # 184227)[3] digested with restriction enzyme NdeI and HindIII (NEB). All sequences were confirmed by sanger sequencing (Azenta) with T7 primer.

1.3 His-AviTag-CCs expression and purification.

For His-AviTag-CC protein expression, DNA constructs were introduced into BL21-CodonPlus(DE3)-RIPL *Escherichia coli* (*E. coli*) (Agilent) by heat shock transformation. Cells were cultured in 10 ml (Luria-Bertani, Miller) media with 50 mg/L Kanamysin at 37 °C and shaken at 220 r.p.m. overnight. The 10ml culture was then transferred to inoculate 1 liter LB with 50 mg/L Kanamysin, which was grown at 37 °C with 220 r.p.m. shaking until OD600 = 0.6. IPTG (isopropyl β-D-1-thiogalactopyranoside; Millipore Sigma, #I5502) was added to the culture to a final concentration of 0.2 mM, and the culture was transferred to 18 °C for continued shaking at 220 r.p.m. overnight. Cells were harvested by centrifugation at 8,000 r.p.m. at 4 °C. Pelleted cells were lysed in B-PER™ Complete Bacterial Protein Extraction Reagent (Thermo Fisher Scientific, #89821) supplemented with Halt™ Protease Inhibitor Cocktail (Thermo Fisher, #78430) for 15 min at room temperature, then clarified by centrifugation at 15,000 g for 10 min. One fourth volume of 5X (50 mM imidazole, 250 mM Tris×HCl, 2.5 M NaCl, pH = 7.5) wash buffer was added to supernatant to reach 1X concentration. The Ni-NTA bead slurry (Themo Fisher Scientific, #R90115) was added to gravity columns and equilibrated with 10 gel volumes of 1X wash buffer. Protein was added to the column after equilibration and was then washed with 20 gel volumes of 1X wash buffer. Subsequently, 2 gel volumes of elution buffer (1M imidazole, 50 mM Tris×HCl, 500 mM NaCl, pH = 7.5) was added. The eluents were filtered using a 0.2µM syringe (Fisher Scientific, #09-720-004) to remove any residual resin and concentrated with a Pierce™ Protein Concentrators PES, 3K MWCO, 2-6 ml (Thermo Fisher #88515) to a concentration of 20 mg/ml.

1.4 Cell culture and transfection.

Cell lines vinculin-null, MEF WT were cultured in complete growth medium (DMEM (Corning, #10-013-CM) supplemented with 10% fetal bovine serum (FBS; Corning, #35-015-CV), 1% MEM Non-Essential Amino Acids (Thermo Fisher Scientific, #11140050), 1% HEPES (Thermo Fisher Scientific, #15630080), and 1% Antibiotic Antimycotic Solution (Sigma-Aldrich, #A5955)). For live-cell imaging, imaging medium (Medium 199, no phenol red (Thermo Fisher Scientific, #11043023) supplemented with 10% fetal bovine serum (FBS;

Corning, #35-015-CV), 1% MEM Non-Essential Amino Acids (Thermo Fisher Scientific, #11140050), 1% HEPES (Thermo Fisher Scientific, #15630080), and 1% Antibiotic Antimycotic Solution (Sigma-Aldrich, #A5955)) was used. For transient transfection, cells in antibiotic free media (DMEM (Corning, #10-013-CM) supplemented with 10% fetal bovine serum (FBS; Corning, #35-015-CV), 1% MEM Non-Essential Amino Acids (Thermo Fisher Scientific, #11140050), and 1% HEPES (Thermo Fisher Scientific, #15630080)) with 50% confluency were transduced with Lipofectamine 3000 (Invitrogen, #L3000001) using opti-MEM (Thermo Fisher Scientific, #A4124801) for 24h before seeded on imaging dish.

1.5 Fluorescence microscopy of cultured cells.

35 mm cell imaging dish with a glass bottom (ibidi, #81218-200) was coated with 10 µg/ml fibronectin (Thermo Fisher Scientific, #F1141) or 0.01% poly-*L*-lysine (CAS-25988-63-0, Sigma-Aldrich P4707) at 4ºC overnight. On the day of imaging, the coated dishes were washed with imaging media three times before seeding cells. Vinculin null cells transfected with TS or Fi constructs were plated at a density of 1×10^5 cells/dish and incubated at 37 °C under 5% CO2 in T25 flasks in complete growth medium for 4h before imaging. Images were acquired on a Nikon Ti2 Eclipse confocal microscope (Minato City, Tokyo, Japan) using a 100× oil objective, reflective interference contrast microscopy (RICM), Nikon Elements, perfect focus, epifluorescence illumination, and three-cubes for sensitized emission acquisition. The filter sets for the three cubes included donor channel FITC ex: ET470/40x, em: ET525/50m, dichroic (T495lpxr); acceptor channel TRITC, ex: ET545/25x, em: S605/70m, dichroic (T565lpxr); and the FRET channel, Clover ex: ET470/40x, mRuby2 em: ET605/70m, dichroic (T565lpxr) from Chroma Technology (Bellows Falls, VT, USA). The exposure for sensitized FRET acquisitions was set at 1500 ms for all channels. Images were analyzed using ImageJ.

1.6 Sensitized Förster resonance energy transfer index analysis.

Image processing was performed using ImageJ and optimized as described in Sharma et al.[4] The correction factors were calculated as shown in **E1-E3**. *A* represents the fluorescence intensity from donor (Clover) channel, *B* represents the fluorescence intensity from FRET channel, and *C* represents the fluorescence intensity from acceptor (mRuby2) channel FRET channel. *b* was calculated through cells transfected with Clover expression plasmid (Addgene, plasmid # 40259), *g* was calculated through cells transfected with mRuby2 expression plasmid (Addgene, Plasmid # 40260). FRET crosstalk was not observed. These values were empirically calculated for our system using our specific microscope and filter setup. Note that FRET index was used in all our measurement with the exception of the bulk FRET measurements conducted using a fluorometer using isolated tension sensors (see 1.11).

Clover Crosstalk	$$\beta = \frac{B}{A}$$	ES1
mRuby2 Cross-Excitation	$$\gamma = \frac{B}{C}$$	ES2
FRET index	$$FRET_{index} = \frac{B - A \times \beta - C \times \gamma}{C}$$	ES3

ImageJ macro scripts:

```
macro "FRET" {
    run("Images to Stack", "name=Stack title=[] use keep");
    setOption("ScaleConversions", true);
    run("StackReg ", "transformation=[Rigid Body]");
    run("Stack to Images");
    selectWindow("D");
    close();
    selectWindow("A");
    close();
    selectWindow("F");
    close();
    run("Subtract Background...", "rolling=20");
    selectWindow("A");
    run("Subtract Background...", "rolling=20");
    selectWindow("F");
    run("Subtract Background...", "rolling=20");
    selectWindow("A");
    run("Duplicate...", " ");
    //run("Brightness/Contrast...");
    run("Enhance Contrast", "saturated=0.35");
    run("CLAHE ", "blocksize=19 histogram=256 maximum=6");
    run("Exp");
    setAutoThreshold("Default dark");
    //run("Threshold...");
```

```
        setThreshold(300, 65535);
        run("Create Selection");
        run("Make Inverse");
        roiManager("Add");
        selectWindow("D");
        roiManager("Select", 0);
        setBackgroundColor(0, 0, 0);
        run("Clear", "slice");
        selectWindow("A");
        roiManager("Select", 0);
        run("Clear", "slice");
        selectWindow("F");
        roiManager("Select", 0);
        run("Clear", "slice");
        run("Image Expression Parser (Macro)", "expression=((A-C*0.1186-B*0.044)*100)/B a=[F] b=[A] c=[D] d=None e=None");
        run("royal");
        setMinAndMax(0, 45);
}
```

1.7 Molecular Dynamics (MD) Protocol:

All MD simulations were performed using NAMD,[5] with the CHARMM36m force field for proteins and the TIP3P water model.[6,7] Langevin dynamics (damping constant 1.0 ps^(-1)) enforced a constant temperature of 310 K, and an anisotropic Langevin piston barostat maintained a pressure of 1 atm.[8] Bonded interactions and short-range nonbonded interactions within a 12 Å cutoff were calculated each timestep. Long-range electrostatics were managed via the Particle Mesh Ewald (PME) method, updated every two timesteps.[9] VMD was used to perform all visualization and analyses.[9]

1.8 Primer modification and purification.

Forward primer 5'-/5AmMC6/GT CTG AGC GGT TCA ACA GGG GCC GCG GGT-3' and reverse primer 5'-/5AmMC6/CT AA/iUniAmM/ AAA ACC AAG GGA AAG AAG ACT TAA A-3' for multiplying DNA handle were custom synthesized by Integrated DNA Technologies. The 5' of forward primer was modified with tetrazine and reverse primer was modified with bis-azide. Products were purified using HPLC.

1.9 Assembling biotin-protein–DNA conjugates.

A 2326 bp long DNA handle was amplified using Q5® High-Fidelity PCR Kit (NEB) with Tetrazine modified forward primer, azide modified reverse primer and lambda-DNA (NEB) vector. Purified His-AviTag-CCs were first biotinylated by BirA ligase (BirA500-RT: BirA biotin-protein ligase lyophilized reaction kit; Avidity). The BirA ligation reaction was conducted with 1μg BirA ligase every 10nmol protein, followed my manufacture protocol. The biotinylated CCs were then reduced by immobilized TCEP disulfide reducing gel (Thermo Fisher, #77712) to eliminate oligomerization via terminal cysteines and then incubated with TCO-maleimide for 4h to introduce TCO to the terminal cysteine residue. Subsequently, freshly made bio-CC-TCO was incubated with Tz-DNA-Azide for 1h and was stored at 4ºC. 2.34 μm SPHERO™ Jeffamine Polystyrene beads (Spherotech, JAP-10-5) were washed five times with DMSO, then incubated with NHS-DBCO for 1h followed by another five times washing with DMSO. Protein-DNA sample was clicked to DBCO functionalized beads in 1X PBS (pH 7.4).

1.10 Single-molecule force spectroscopy calibration.

C-Trap laminar flow channels were washed followed by manufacture protocol and filled with 1X PBS after wash. 1.36 μm Streptavidin (SA) beads (Spherotech, SVP-15-5) were injected to channel 1, 2.34 μm DBCO functionalized beads conjugated with protein-DNA sample was injected to channel 3 (all beads were diluted in 1X PBS). CC-S_0 and CC-S_2 constructs were suspended between a DBCO/SA bead pair and the position of the two beads were controlled and read out using Lumicks software. CC was unfolded and refolded in stretch–relax cycles by changing the trap distance with a velocity of 50 nm/sec.

1.11 FRET efficiency calculations from spectrofluorometry.

Hypotonic lysates were prepared from HEK293 cells as previously described (Chen et al., 2005).[10] Same density of lysates from untransfected cells were used as a reference background. Spectrofluorometric measurements were made with Horiba Scientific fluorometer with a with 0.55 s integration time and high gain for all samples. Spectra were traced from 520 to 700 nm following donor excitation at 505 nm (λ_{Dex}), and from 590 to 700 nm following acceptor excitation at 575 nm (λ_{Aex}). FRET efficiency was calculated as:

$$E = \frac{\varepsilon_{A\,(575\,nm)}}{\varepsilon_{D\,(505\,nm)}} \left(\frac{I_{f\,(610\,nm)}}{I_{a\,(610\,nm)}} - \frac{\varepsilon_{A\,(505\,nm)}}{\varepsilon_{A\,(575\,nm)}} \right) \qquad \text{ES4}$$

I_f and I_a are the intensities, at peak acceptor emission wavelength (λ_{Aem} =610 nm), of the sample excited at donor and acceptor wavelengths, respectively. Donor and acceptor molar extinction coefficients (ε_D and ε_A, respectively) at specified wavelengths (λ_{Dex} and λ_{Aex}) were calculated from absorbance spectra measured on the same spectrofluorometer in absorbance mode using FPbase previously-measured maximal extinction coefficients: $\varepsilon_D{}_{(505\,nm)}$=111,000 M^{-1}cm^{-1} for Clover, and $\varepsilon_A{}_{(575\,nm)}$=113,000 M^{-1}cm^{-1} for mRuby2.[11,12]

S2. Supplementary note 1. Role of CC orientation in CCTS

To investigate the role of CC orientation in CCTSs, we first tested vinculin activity upon insertion of CC structures that fold into parallel (shearing) and antiparallel (unzipping) geometries (**Supplementary Note 1 Figure 1a**). CCs tagged with fluorescent proteins were inserted between the vinculin head and tail domains as this site has been used in past studies and serves as a validated test-bed model for developing new GETS (**Scheme 1d**).[2,13] We initially designed and investigated three constructs that were inserted into vinculin (**Supplementary Note 1 Figure 1b**). The first two constructs employed a parallel CC (GCN4), that linked each a-helical segment by either a GGS_{12} or a GGS_3. The 12 mer GGS linker allows for dimer formation in the parallel geometry, while the 3 mer GGS linker is too short and thus inhibits intramolecular folding of the CC domain. The third construct, $CC-S_0$, folds in an antiparallel geometry. These three constructs were chosen based on prior literature that measured CC unfolding forces of ~10 pN which is greater than reported vinculin tension of 1-6 pN.[14] Our first goal was to investigate vinculin activity and potential condensate formation as a recent report by Ren et al. demonstrated that CC dimers in parallel and antiparallel geometries form protein condensates in yeast upon experiencing sufficient unfolding forces[15]. Since condensate formation is likely to inactivate vinculin function, we first tested whether these CC motifs form condensates and interfere with FA formation and cell spreading.

After transfection of vinculin-null mouse embryonic fibroblast (MEF) with CC encoded vinculin, we analyzed the spreading phenotype and evaluated the morphology of FAs (**Supplementary Note Figure 1b**). As expected, vinculin-null MEF cells showed limited cell spreading area, while the same cells transfected with vinculin-venus showed enhanced cell spreading area and elongated FAs (**Supplementary Note 1 Figure 1b,c**). Vinculin-null MEF cells transfected with GCN4-$(GGS)_{12}$-vinculin displayed similar spreading as that of the vinculin-venus control cells, while the GCN4-$(GGS)_3$-vinculin construct showed perturbed cell adhesion and formation of protein condensates (**Supplementary Note 1 Figure 1b,c**). Validating this result, we found greater circularity for GCN4-$(GGS)_3$-vinculin signal compared to that of the GCN4-$(GGS)_{12}$-vinculin (**Supplementary Note 1 Figure 1d,e**, see detailed work flow in **Supplementary Note 1 Figure 2**). These data indicate that the GCN4-$(GGS)_3$ construct (unfolded parallel CCs) promotes intermolecular assembly of CCs thus driving aggregate formation (**Supplementary Note 1 Figure 1f**). In contrast, the $CC-S_0$ vinculin construct which adopts an anti-parallel unzipping geometry showed normal cell adhesion as indicated by cell spreading area (**Supplementary Note 1 Figure 1b,c**).
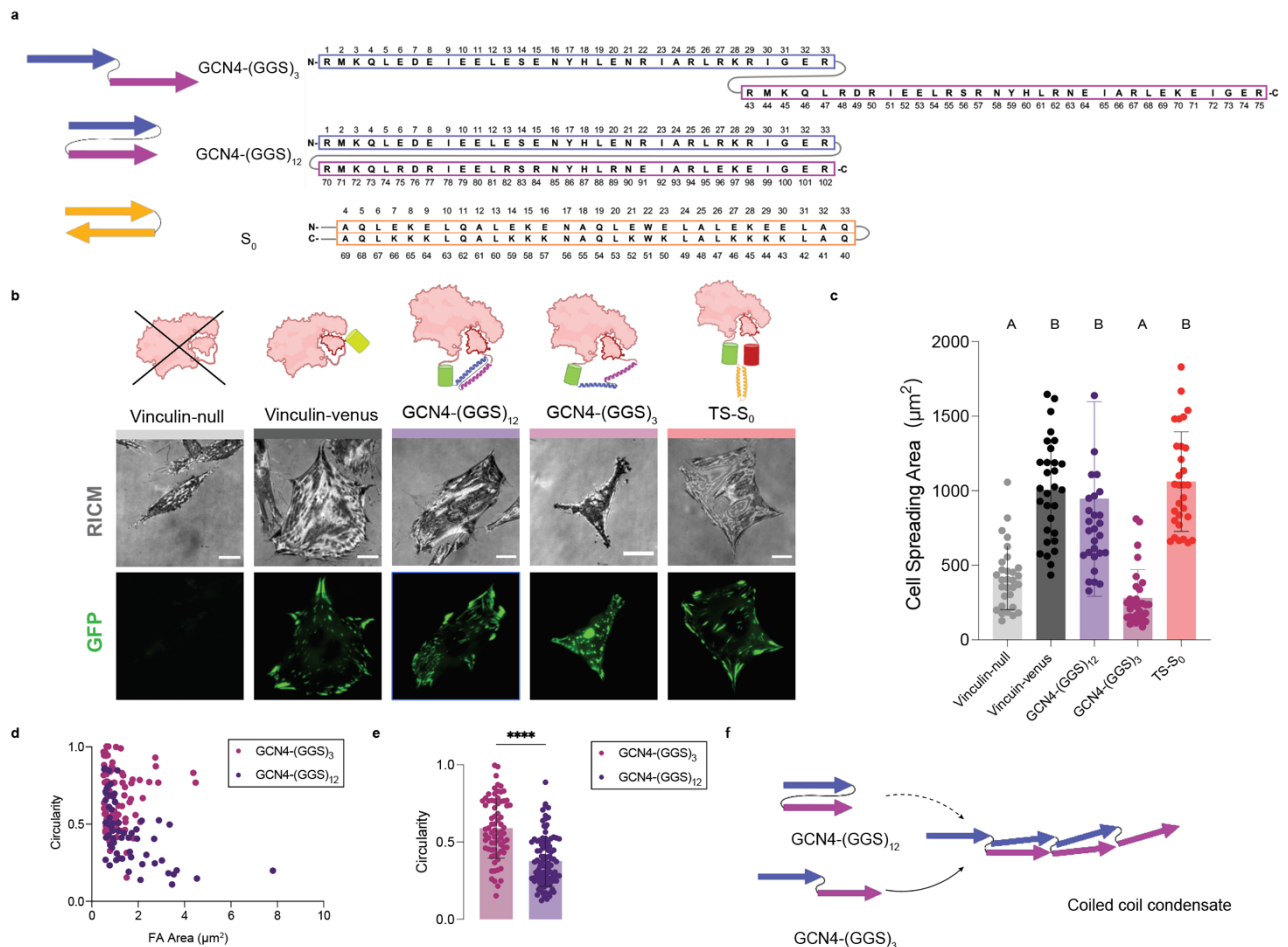

Supplementary Note 1 Figure 1. Anti-parallel CCTS better preserves vinculin function. (a) Sequence of parallel coiled-coil GCN4 with short linker $(GGS)_3$ or long linker $(GGS)_{12}$ and sequence of antiparallel $CC-S_0$. (b) Illustrations of vinculin constructs (top), RICM images (middle, gray), and GFP-fluorescence images (bottom, green) of MEF cells with vinculin null, vinculin-venus, vin-GCN4-$(GGS)_{12}$, vin-GCN4-$(GGS)_3$, and vin-$CC-S_0$. (c) Plot of cell spreading area for (b). Data labeled with

different letters are significantly different from each other (p < 0.0001). (n=30). (d) XY-plot for circularity of fluorescent vinculin signal against its area (μm^2) for MEF cells with vin-GCN4-(GGS)$_3$ and vin-GCN4-(GGS)$_{12}$. (n=88 and 62, respectively) (e) Plot analysis of circularity of fluorescent vinculin signal of its area >1 μm^2 for MEF cells with vin-GCN4-(GGS)$_3$ and vin-GCN4-(GGS)$_{12}$. (n=74 and 98, respectively) **** p < 0.0001, unpaired t-test, two-tailed, assuming unequal SD. (f) Illustration of protein condensate formation driven by intermolecular coiled-coil interactions in unfolded conformation.

Given that the unfolded CCs in the parallel geometry forms aggregates and hinder cell adhesion, this suggests that parallel CC tension sensor will likely perturb vinculin function forming condensates which is consistent with Ren et al.'s observations.[16] Hence, we next focused our efforts on designing CCTS structures in an antiparallel unzipping geometry to preserve vinculin function. Importantly, another advantage of the antiparallel geometry is that it allows the N and C termini to minimize their distance upon folding and conversely to maximize distance following mechanical unfolding, which is desirable for enhancing FRET S/N for readout of tension.
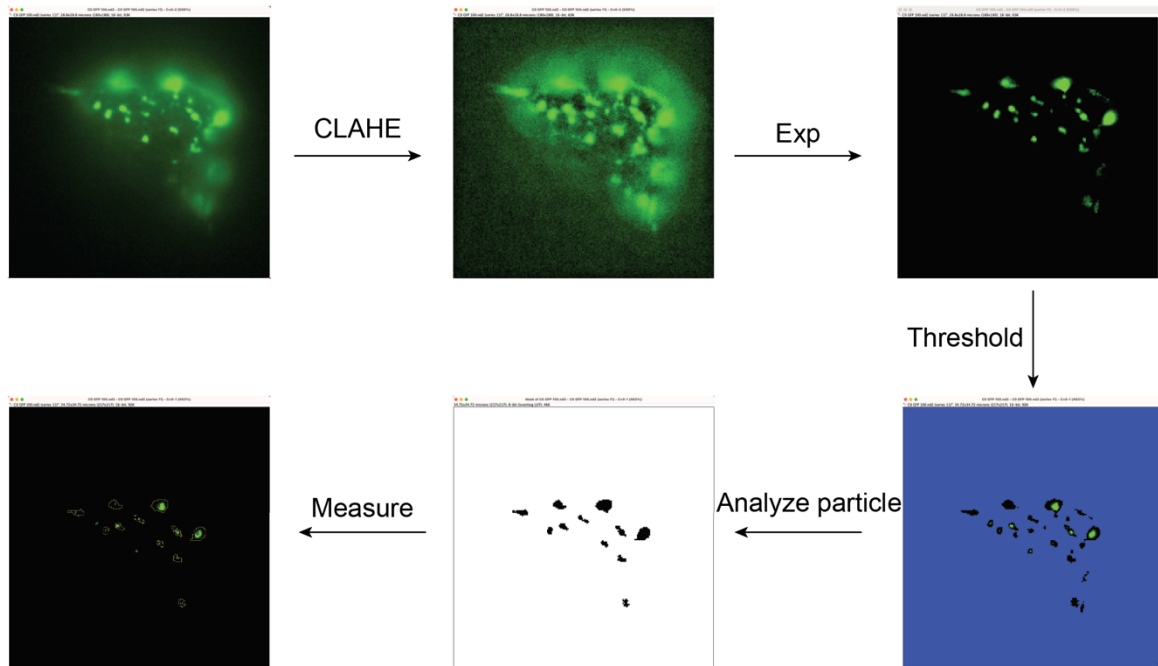
Supplementary Note 1 Figure 2. Analysis of vinculin circularity. Image from GFP channel was processed from ImageJ plugin CLAHE to enhance the contrast. Then the pixel value was exponentiated, and threshold to 300-65533 to select areas with high fluorescent intensity which represent high concentration of local vinculin. Next, ImageJ plugin analysis particle was used to measure the circularity.

To analyze the vinculin fluorescent area at the cell spreading surface, we used ImageJ plugin CLAHE to enhance the contrast, then exponentially adjusted the pixel values to further enhance the contrast. Then threshold was set to [300, 65533] to eliminate background pixel values to select each separate vinculin areas. ImageJ built in plugin "analyze particles" was then conducted to the image and recognized how many different vinculin areas are there. Finally, we measured the recognized areas and obtained circularity data.

S3. Supplementary note 2. Molecular dynamics simulation of coiled-coil stability.

3.1 System Construction:

The wild-type coiled-coil (CC-S_0) structural model was predicted using AlphaFold2, with most residues exhibiting 'very high' confidence scores. Mutant coiled-coil structures (CC-S_1, CC-S_2, CC-S_4, CC-S_7) were generated by serine substitution of specific hydrophobic residues in the CC-S_0. The N-terminus and C-terminus of the proteins were capped with acetyl (ACE) and N-methyl (CT3) groups, respectively. Proteins were solvated in an 80 Å cubic box with ~62,000 water molecules, and 0.15 M NaCl was added for neutralization and to mimic physiological ionic strength. The final systems, each comprising ~48,000 atoms, were assembled to assess the impact of sequence variations on the coiled-coils' unfolding energy.

3.2 System Equilibration:

All systems were equilibrated using a 2 fs timestep via sequential relaxation of components. Initially, water and ions were equilibrated with the protein restrained for 1 ns. Subsequently, protein sidechains were relaxed for 5 ns, followed by the entire system for an additional 5 ns. Prior to each equilibration step, 2000-step energy minimizations were conducted. To mitigate termini fluctuations and ensure cross-system consistency, N and C termini backbones were restrained to continue the coiled-coils' helical structure.

3.3 Steered Molecular Dynamics (SMD):

SMD was utilized to ascertain the PMF to unzip coiled-coil structures. The reaction coordinate was defined as the distance between the mass centers of the N termini's acetyl group and the C termini's methylamine group. Secondary structure restraints with a force constant of 100 kcal/mol were applied to prevent helical denaturation, a common artifact of simulation rates surpassing experimental loading rates.[17] The coiled-coils were stretched from 13 Å to 63 Å over 400 ns employing Hydrogen Mass Repartitioning (HMR) and a 4 fs timestep, reaching a loading rate of 1.5×10^7 nm/s. This rate was sufficiently slow to show same magnitude of forces as observed in single-molecule force spectroscopy, yet fast enough to allow for multiple replica simulations to reach adequate convergence. A total of 10 replicas are performed for each system to record the accumulated works, which are combined to get the PMF according to the Jarzynski Equality.[18]

To establish an appropriate number of replicas necessary for robust convergence across all systems, we conducted a series of convergence tests using the CC-S_2 variant. A total of 19 replicas of SMD simulations were carried out on CC-S_2 (**Supplementary Note 2 Figure 1**). From this pool of 19 curves, we performed ten independent random selections of subsets consisting 2, 5, and 10 replicas, and calculated the combined accumulated work as the PMF for each selection according to the Jarzynski Equality.[18] The resulting curves of the 2-replica and 5-replica subset selections displayed considerable variability, indicating that such small numbers of replicas did not achieve convergence. In contrast, the 10-replica selections showed a narrow distribution in the accumulated work, closely approximating the PMF of the full 19-replica set, with the difference within ±1 kcal/mol. This level of consistency in the 10-replica subsets validates the use of 10 replicas for estimating the PMF across all systems, providing a balanced approach between computational resource expenditure and data reliability.
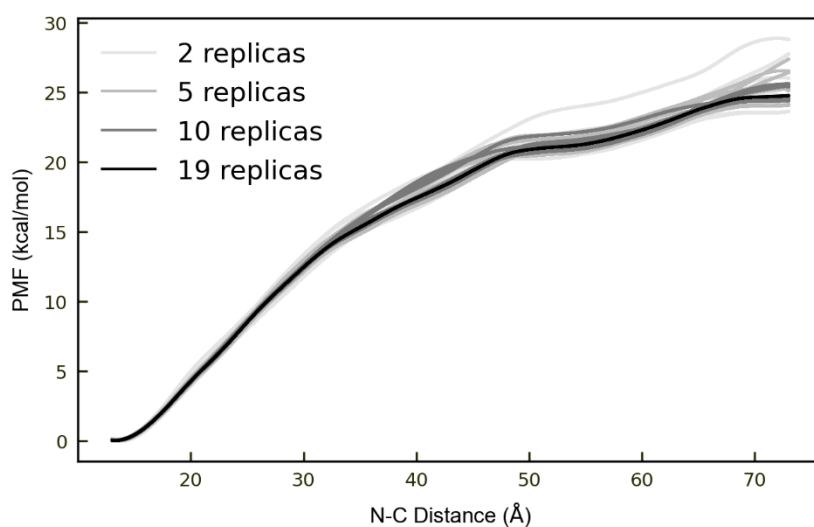

Supplementary Note 2 Figure 1. Convergence test on CC-S2 with a total of 19 replicas of SMD simulations performed. The PMF of unfold the CC calculated from the full set of 19 replicas, comparing with PMF combined from ten random subset selections of 2, 5, and 10 replicas, respectively. The wider distribution of the 2-replica and 5-replica subset selections indicates insufficient convergence, while the 10-replica subset selections closely approximate the 19-replica set (±1 kcal/mol), suggesting that 10 replicas provide a reliable estimation of the PMF.

S4. Supplementary note 3. Analysis of Single-molecule Optical Tweezer Data:

CC-S_0 and CC-S_2 constructs were suspended between a DBCO/streptavidin bead pair and the position of the two beads were controlled and read out using Lumicks software. Briefly, adjusting the relative position of the beams trapping the bead pair allowed for varying force to be applied on the tethered molecule, while readouts of the beam positions' and the beads' displacement from their corresponding trap center gave distance and force readouts, respectively. The beads were positioned < 500 nm from each other (shorter than the expected length of the 2326 bp handle, such that no external force was being applied), and then moved at a constant rate of 50 nm/sec away from each other until a transition event was observed. Such an event can be observed by plotting the observed force applied on the construct against the bead pair's positional difference, as shown in the representative force-distance curve (FD curve, **Supplementary Note 3 Figure 1**). Under this experimental geometry the construct started in low-force state and underwent a transition upon application of high-force, so this trace was labeled an "opening trace". After opening the construct through external force, the experiment was performed in reverse order, with the construct starting with applied high-force (opened state) and the beads monotonically moving closer resulting in a transition towards a low-force state (closed state), termed a "closing trace". For each data set (S_0 and S_2 constructs), two different molecules were trapped (N=4 molecules) and repeat opening/closing measurements were performed across all molecules (N=46 events).
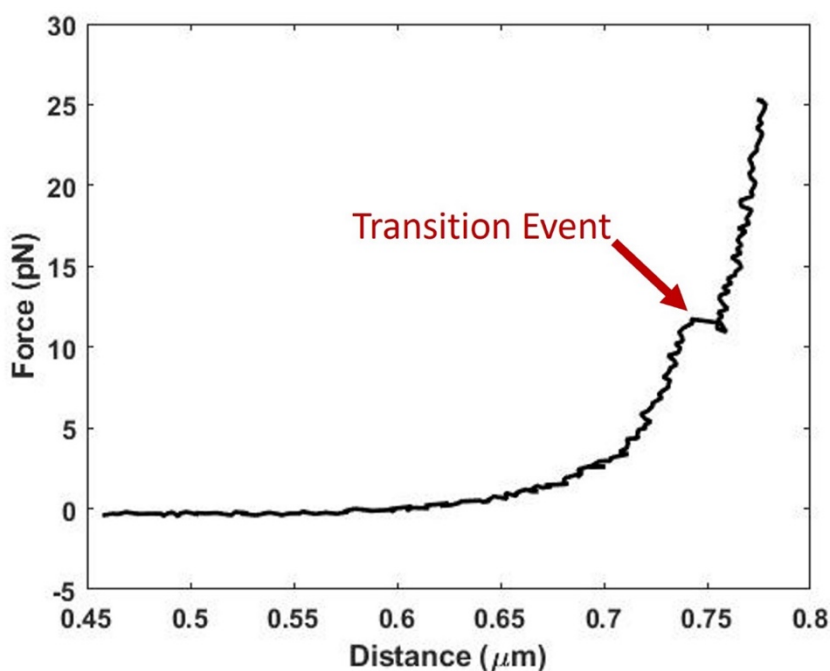
Supplementary Note 3 Figure 1. Representative FD curve for an opening event. The transition of the CCTS structure from closed-form to opened-form can be qualitatively observed and is marked with a red arrow.

There were four goals in our single-molecule analysis, which are outlined in S4 section:

1. Systematically identify the transition points of the FD curves
2. Identify the force thresholds corresponding to each opening or closing transition
3. Fit the Fd curves to an extensible wormlike chain model
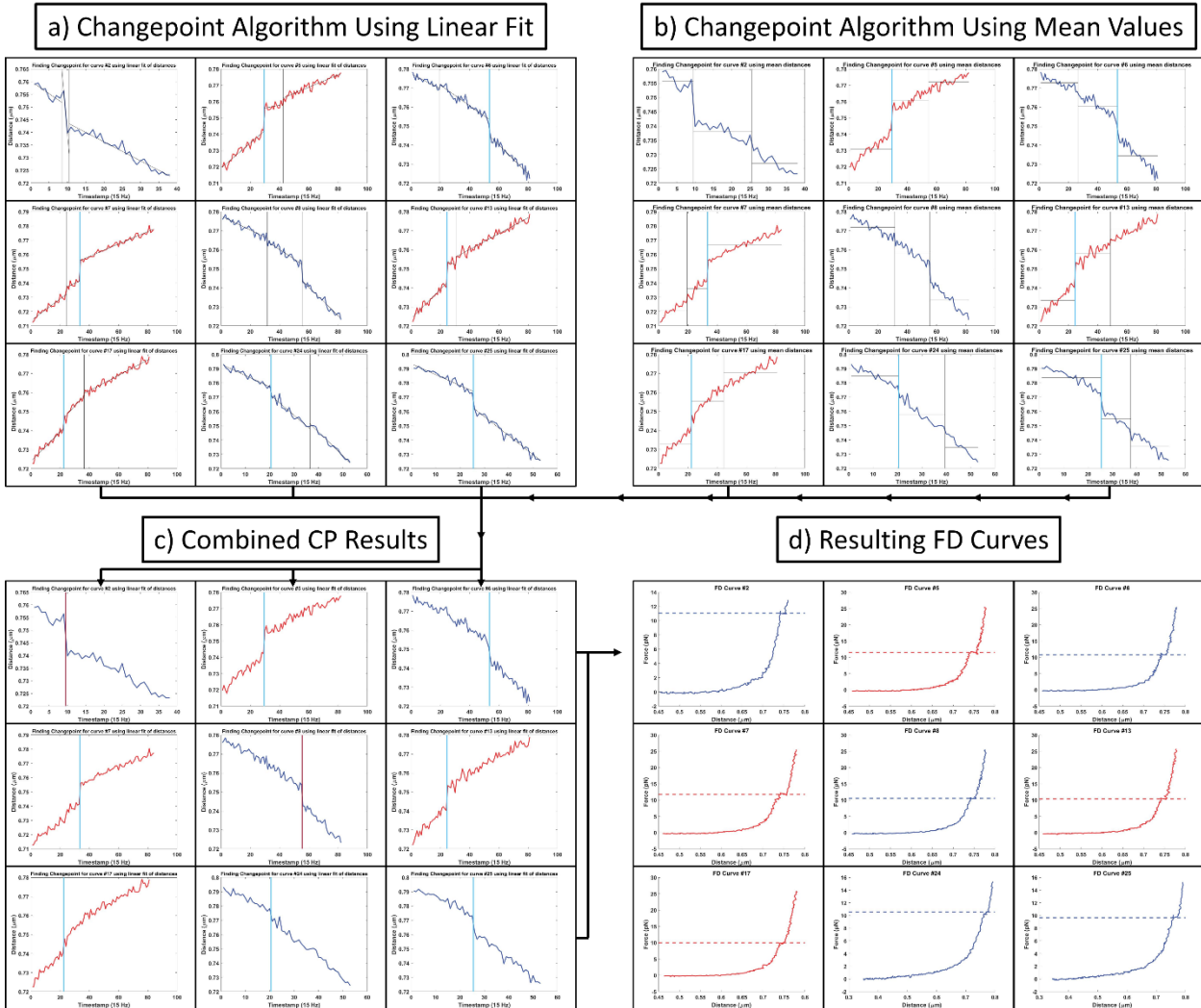4. Identify the distal change that accompanies the opening/closing transitions of the CCTS probe

4.1 Identifying the transition points within the FD curves

Custom Matlab codes were written and used on each FD curve independently to obtain the transition point within each curve, and the methodology is as follows. Intuitively, a transition between opened and closed states of the CCTS probe would result in a large shift in measured *distance* between the two endpoints (**Supplementary Note 3 Figure 1**) during timepoints of force being applied. Thus, timestamps with a range of forces (5-25 pN, containing all transition points) were selected and the FD curves were plotted as distance-time curves, where the distance between the two beads is plotted as a function of time (**Supplementary Note 3 Figure 2**). Each curve contained between 38-86 data points, thus the point with the fewest data points (top left of each 3x3 grid, curve #2) and 8 randomly selected FD curves were chosen as representative plots. Some representative plots correspond to an opening trace (red) while others correspond to a closing trace (blue), with colors matching **Figure 4**.

a) Raw Force-Distance Curves

b) Distance-Timestamp Curves within force range
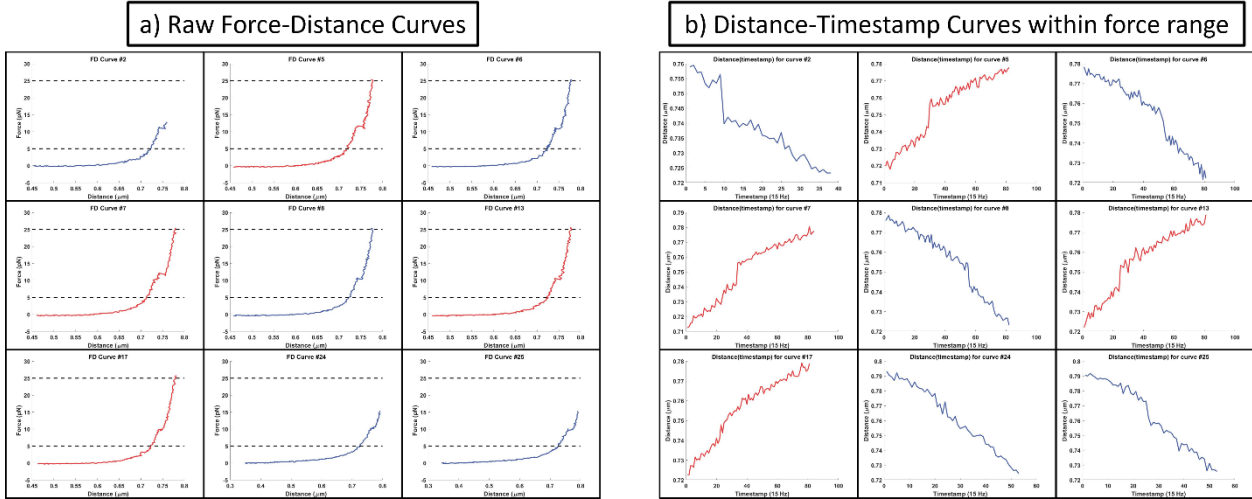
Supplementary Note 3 Figure 2. Red and blue colors of traces correspond to an opening and closing motion to induce transition, respectively. a) Raw data of the force-distance, with force range of 5-25 pN highlighted with the dotted black line. Opening and closing traces are marked in red and blue, respectively. b) Corresponding distance-timestamp curves for all points within the 5-25 pN range.

a) Changepoint Algorithm Using Linear Fit

b) Changepoint Algorithm Using Mean Values

c) Combined CP Results

d) Resulting FD Curves

Supplementary Note 3 Figure 3. a) Results on the representative traces of using a changepoint algorithm based on linear fitting of the distance-time curves. Vertical gray lines represent the changepoint index and diagonal gray lines represent the linear fits. A blue vertical line represents a single matching changepoint detected between the linear-based and mean-based changepoint algorithms. b) Results from the mean-based changepoint algorithm. Horizontal gray lines represent the mean value of data between changepoints. c) Combined results of both changepoint algorithms. Vertical blue lines represent a single matching changepoint between the two algorithms. Vertical red lines represent that a single match was not found (<25% of cases) and a linear changepoint algorithm with a maximum of 1 changepoint was run to find a single changepoint. d) results from the changepoint analysis showing the detected force of the transition event.

10

As mentioned, one would expect that the transition point is marked by a sudden increase or decrease in distance for an opening or closing event, respectively. Thus, it is intuitive to identify such an event with a changepoint algorithm which finds a change in the mean distances before and after said changepoint.[19] However, since the experimental conditions involve a constant change in the distance between beads (observe the mostly-constant slope of many distance-time curves in **Supplementary Note 3 Figure 2b**), it can also be said that a changepoint in a slope-fitting of the distance curves can be used to systematically detect the transition point. Such methods of utilizing a derivative have been reported before for similar optical tweezer-based experiments.[20,21] For our purposes, we found combining results from both changepoints (linear fit and mean values) gave qualitatively best results and helped overcome the not-insignificant noise in some of our single-molecule traces (e.g. bottom left and bottom center curves in **Supplementary Note 3 Figure 3**). Briefly, every curve was fit with both changepoint algorithms allowing a maximum of two detectable changepoints (**Supplementary Note 3 Figure 3a,b**). All vertical lines, as well as slope fits (**Supplementary Note 3 Figure 3a**) or average values (**Supplementary Note 3 Figure 3b**) are marked in grey, except when there is a single matching changepoint identified by both algorithms where that changepoint is marked in light blue. For >75% of the curves a singular matching changepoint (blue line) was detected and selected as the transition point for the FD curve. Cases where there was not 1 total matching changepoint between both algorithms meant there were either 0 matches (**Supplementary Note 3 Figure 3** top left corner) or two matches (**Supplementary Note 3 Figure 3**, center). For these two representative curves this was due to a slower transition which encompassed several points (top left) or the algorithms matched completely (center). In all cases fitting the curves with a linear changepoint algorithm constrained to 1 maximum changepoint was used to find the final changepoint (visualized in **Supplementary Note 3 Figure 3** with a vertical red line). Lastly, these indexes of this transition point was matched to its corresponding force value and plotted on top of the FD curve (**Supplementary Note 3 Figure 3d**).

4.2 Analyzing the force thresholds corresponding to CCTS open/close transitions

Once all force thresholds for transitions had been identified (**Supplementary Note 3 Figure 3d**) the distributions were further analyzed. The values for each construct (CC-S_0 and CC-S_2) across all single-molecule experiments were summed together while keeping transitions for the opening and closing traces distinct (**Supplementary Note 3 Figure 4**). These distributions were then fit to Gaussians (**Supplementary Note 3 Figure 4**). Note, slight differences in the Fd curve shape (such as in **Supplementary Note 3 Figure 4**) are due to heterogeneity in bead size. The approach to compensate for the difference in bead size is compensated for is described at the end of **Supplementary Note 3**.
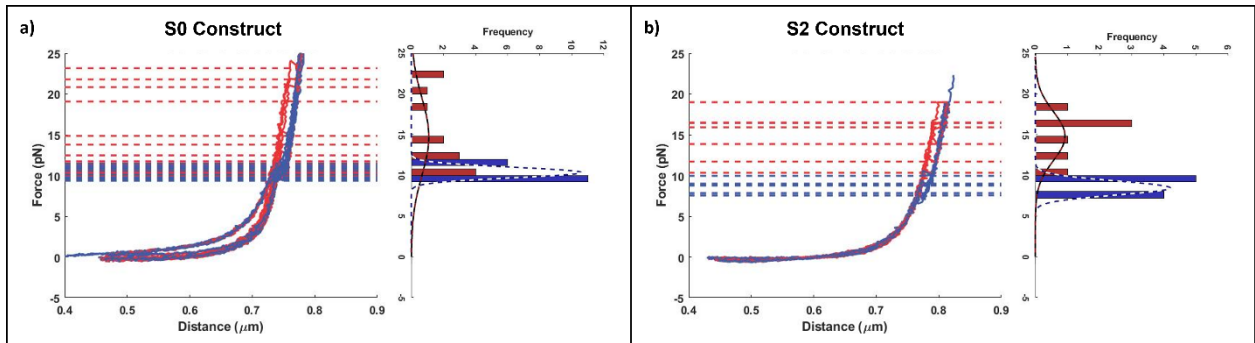
Supplementary Note 3 Figure 4. All single-molecule optical tweezer traces for CC-S_0 (a) and CC-S_2 (b) constructs. Opening traces are shown in red while closing traces are shown in blue. The distribution of the force thresholds is shown in the histogram to the right of the traces, with the force-axes aligned. Gaussian fits are overlaid on top of the histograms for the opening (red-black dotted line) and closing (blue-white dotted line) traces.

$F_{1/2}$ was estimated from the intersection of the opening and closing force distributions. Range of intersection given uncertainty in the Opening Forces measurements are shown in **Supplementary Note 3 Figure 5**.
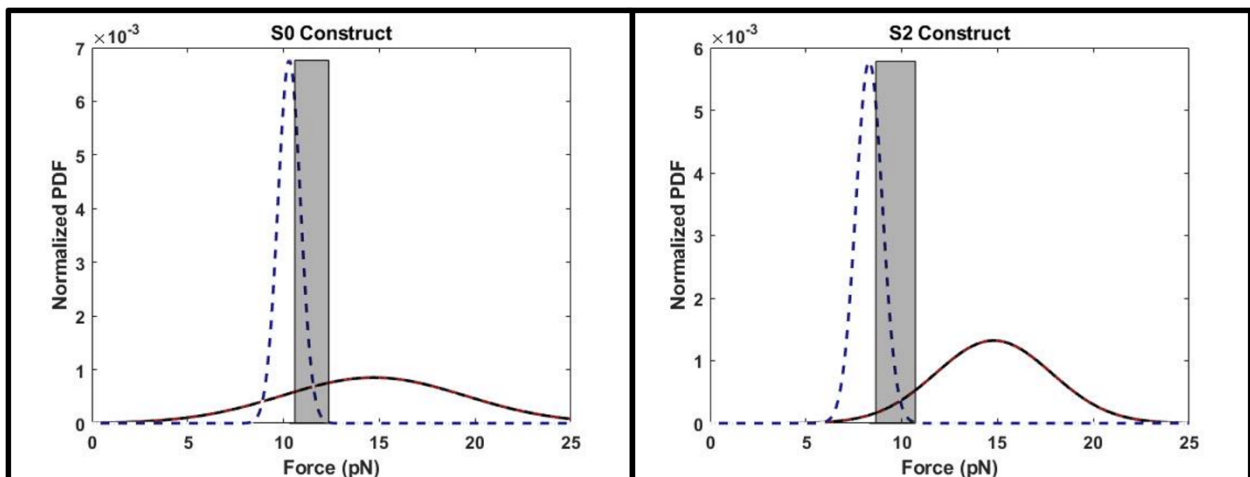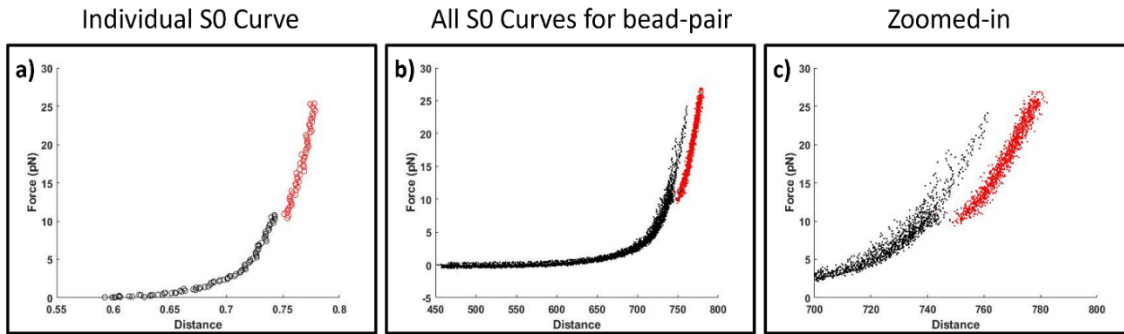

Supplementary Note 3 Figure 5. A graphical representation of the range of intersection ($F_{1/2}$ value) for S_0 (left) and S_2 (right) constructs given uncertainty in the Opening Forces measurements. Probability distribution functions are drawn from the reported values (**Figure 4**), with the gray regions showing a range of 0.5σ-3.5σ for the Closed Forces distribution. This translates to ranges of 10.6–12.4 pN (S_0) and 8.6–10.7 pN (S_2).

4.3 Fitting FD curves to an extensible worm-like chain model.

11

Each single-molecule FD trace is composed of two structures: a closed form and an opened form for each construct. Therefore, the traces are fit to two extensible worm-like chain (eWLC) models, each which models the structures. First, we parsed which data point from each trace belongs to each form. We did so by looking at the timestamp that marks each FD threshold and assigned the data from before/after this timestamp to its corresponding form (**Supplementary Note 3 Figure 6a**). For example, if a FD trace began at low force and transitioned to a higher force (opening trace) the data _pre_ceding the FD threshold timestamp were assigned to the closed form and the data _pro_ceeding the FD threshold timestamp were assigned to the opened form. For FD traces going from high to low forces (closing trace) the assignments were reversed. Lastly, the data from all individual traces for each bead-pair were grouped together, as fitting each trace to two eWLC models independently simply did not provide much data for statistically-valid fits (**Supplementary Note 3 Figure 6b,c**).

Supplementary Note 3 Figure 6. Parsing data from FD traces into closed (black) and opened (red) forms. a) Representative trace showing data split into the two forms based on the timestamp of the transition. b) All data for a bead-pair grouped together. c) Zoomed-in view of plot b.

After parsing the data into the opened and closed form the datasets were fit to an eWLC model described by Odijk and outlined for optical tweezer experiments by M. Wang et. al.[22,23] The curves were fit in Python using PyLake software developed by Lumicks (specifically, we used the function pylake.lakeview.ewlc_odijk_force("data").subtract_independent_offset() + lk.force_offset("data") to fit the data). In the above function "data" referrers to each data set we fit with the eWLC model, and subtract_independent_offset() + lk.force_offset() correspond to vertical and horizontal offsets of the FD curves (compensating for slight calibration differences in each dataset). The model ewlc_odijk_force minimizes the f(d) dependence given by the following:

$$d = L_0 \left[1 - \frac{1}{2} \left(\frac{k_B T}{F L_p} \right)^{\frac{1}{2}} + \frac{F}{K} \right] \qquad \textbf{ES5}$$

Where F is the force and d is the distance (y and x-axes for our FD curves), L_0 is the contour length (the variable we are primarily interested in), L_p is the persistence length, K is the elastic modulus (or the "stretchiness" as force is applied for the probe+handle construct used in the optical tweezer experiment), and $k_B T$ is the Boltzmann's constant times absolute temperature.

4.4 Identifying the distal change between open/closed forms of CCTS probes.
Ensemble datasets for bead pairs which provided the most data for the S_0 and S_2 constructs are shown along with their fits (**Supplementary Note 3 Figure 7**).
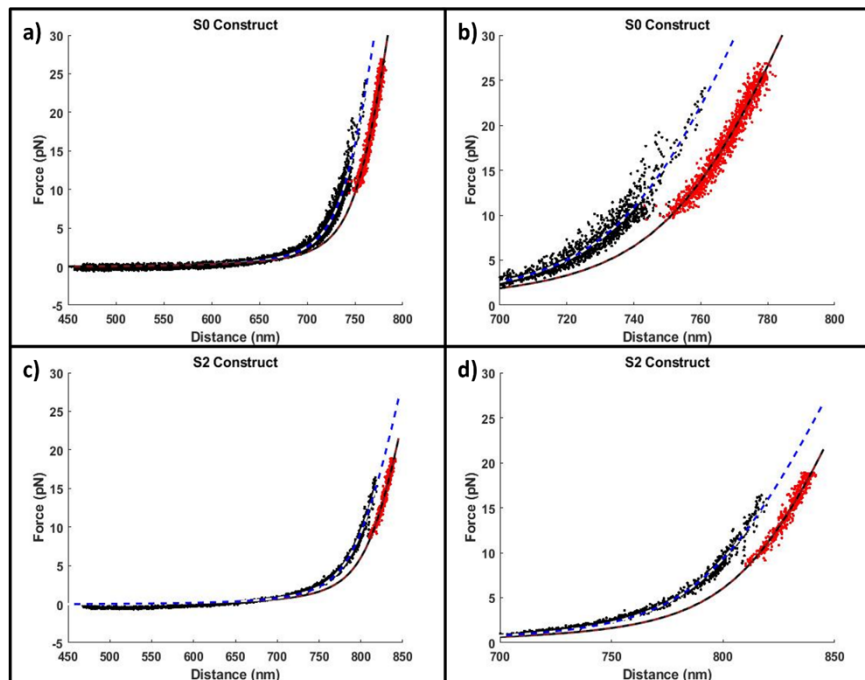
Supplementary Note 3 Figure 7. Ensemble FD trace data sets for bead pairs containing the CC-S_0 (a,b) and CC-S_2 (c,d) construct. Bead pairs were selected based on which pair yielded the largest number of traces. a,b) Closed form data shown as black scatter points with eWLC fits shown as a blue-white dotted line. Opened form data shown as red scatter points with fit in red-black dotted line. Plots are shown at two zoom-levels, with axes scales matching those shown in FigureS16b,c) Data and fits for the CC-S2 construct.

The data for these two fits is tabulated in **Supplementary Note 3 table 1** below:

	CC-S_0-Closed	CC-S_0-Opened	CC-S_2-Closed	CC-S_2-Opened
L_0 (nm)	883.8	902.7	778.4	793.9
L_p (nm)	59.9	56.2	57.0	52.7
K (pN)	516.3	632.5	835.3	864.0

Supplementary Note 3 table 1. Fits for primary variables found in ES5. Values for the contour length (L_0) are highlighted red.

The ΔL values reported in the manuscript are found by taking the difference between the L_0 values for the opened and closed-forms of each construct. The persistence length (L_p) and elastic modulus (K) are comparable to values approximated by Wang et. al. of 50nm and ~720 pN, respectively.[23] It should be noted that, while the $\underline{\Delta}L_0$ values for the CC-S_0 and CC-S_2 are comparable (15 and 19 nm, respectively) the <u>absolute</u> L_0 values vary significantly. This is almost certainly due to the variance in bead sizes, as even measurements of the same construct for different bead pairs have a large variance between absolute L_0 values (**Supplementary Note 3 Figure 8a**). Thus, data for each bead-pair was fit to their own WLC (as differing bead size could result in vastly different L_0 values and curve shapes). Data from each bead-pair fit a WLC model well. Importantly, our measurement is primarily interested in the *difference* between L_0 values for the closed and opened forms, which is independent of the bead size, and can be seen when the FD curves are offset by a constant distance to compensate for this factor (**Supplementary Note 3 Figure 8b**).
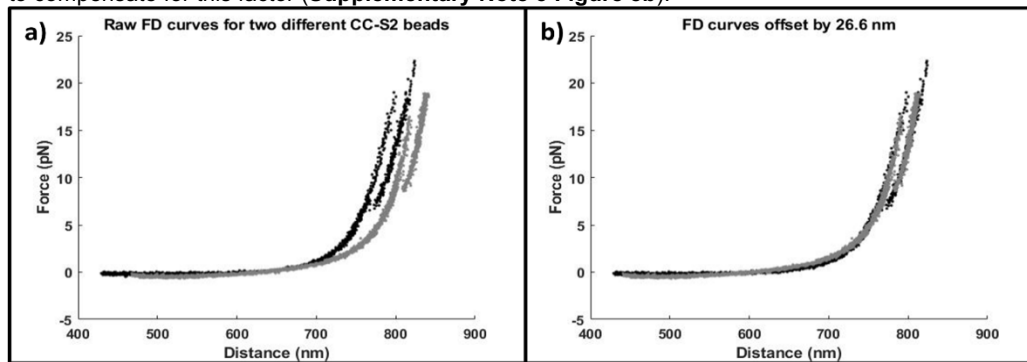
Supplementary Note 3 Figure 8. a) FD curves for CC-S2 construct for two different bead pairs shown in black and gray. b) After offsetting curves by 26.6 nm we can see they follow the same eWLC behavior for the opened and closed forms.

S5: Supplementary Data

Table S1. CC library amino acid sequences.

#	CC name	Sequence
1	S0	GGSAQLEKELQALEKENAQLEWELQALEKELAQGGSGGSQALKKKLAQLKWKLQANKKKLAQLKKKLQAGGS
2	S2	GGSAQLEKELQALEKENAQLEWELQASEKESAQGGSGGSQASKKKSAQLKWKLQANKKKLAQLKKKLQAGGS
3	S4	GGSAQLEKELQALEKENAQSEWESQASEKESAQGGSGGSQASKKKSAQSKWKSQANKKKLAQLKKKLQAGGS
4	S7	GGSAQSEKESQASEKENAQSEWESQASEKESAQGGSGGSQASKKKSAQSKWKSQANKKKSAQSKKKSQAGGS
5	S1	GGSAQLEKELQALEKENAQLEWELQALEKESAQGGSGGSQASKKKLAQLKWKLQANKKKLAQLKKKLQAGGS
6	M2	GGSAQLEKELQALEKENAQLEWEMQALEKEMAQGGSGGSQAMKKKLAQMKWKLQANKKKLAQLKKKLQAGGS
7	Mad	GGSAQLEKEMQALEKENAQLEWEMQALEKEMAQGGSGGSQAMKKKLAQMKWKLQANKKKLAQMKKKLQAGGS
8	E	GGSAQLEKELQALEKENAQLEWELEALEEELAQGGSGGSQALKKKLAQLKWKLQANKKKLAQLKKKLQAGGS
9	M1	GGSAQLEKELQALEKENAQLEWELQALEKEMAQGGSGGSQAMKKKLAQLKWKLQANKKKLAQLKKKLQAGGS
10	Va	GGSAQLEKEVQALEKENAQLEWEVQALEKEVAQGGSGGSQAVKKKLAQVKWKLQANKKKLAQVKKKLQAGGS
11	Ma	GGSAQLEKEMQALEKENAQLEWEMQALEKEMAQGGSGGSQALKKKMAQLKWKMQANKKKMAQLKKKLQAGGS
12	MLMM	GGSAQLEKELQALEKENAQLEWELQALEKELAQGGSGGSQALKKKLAQLKWKLQANKKKLAQLKKKLQAGGS
13	M3	GGSAQLEKELQALEKENAQMEWEMQALEKEMAQGGSGGSQAMKKKLAQMKWKMQANKKKLAQLKKKLQAGGS

Table S2. Plasmid used in this study.

| Plasmid #	Plasmid name	Vector	5' noncoding region	3' noncoding region	Expression in	Antibiotic resistance	Used in
P1	Vh-Clover-CC-S0-mRuby2-Vt	pcDNA3.1(+)	T7	BGH	mammalian expression	Ampicillin	Fig. 2
P2	Vh-Clover-CC-S2-mRuby2-Vt	pcDNA3.1(+)	T7	BGH	mammalian expression	Ampicillin	Fig. 2, Fig. 5, Fig. S10.
P3	Vh-Clover-CC-S4-mRuby2-Vt	pcDNA3.1(+)	T7	BGH	mammalian expression	Ampicillin	Fig. 2
P4	Vh-Clover-CC-S7-mRuby2-Vt	pcDNA3.1(+)	T7	BGH	mammalian expression	Ampicillin	Fig. 2
P5	Vh-Clover-CC-S1-mRuby2-Vt	pcDNA3.1(+)	T7	BGH	mammalian expression	Ampicillin	Fig. 2
P6	Vh-Clover-CC-M2-mRuby2-Vt	pcDNA3.1(+)	T7	BGH	mammalian expression	Ampicillin	Fig. S3
P7	Vh-Clover-CC-Mad-mRuby2-Vt	pcDNA3.1(+)	T7	BGH	mammalian expression	Ampicillin	Fig. S3
P8	Vinculin-Clover-CC-S0-mRuby2	pcDNA3.1(+)	T7	BGH	mammalian expression	Ampicillin	Fig. 2
P9	Vinculin-Clover-CC-S2-mRuby2	pcDNA3.1(+)	T7	BGH	mammalian expression	Ampicillin	Fig. 2
P10	Vinculin-Clover-CC-S4-mRuby2	pcDNA3.1(+)	T7	BGH	mammalian expression	Ampicillin	Fig. 2
P11	Vinculin-Clover-CC-S7-mRuby2	pcDNA3.1(+)	T7	BGH	mammalian expression	Ampicillin	Fig. 2
P12	Vinculin-Clover-CC-S1-mRuby2	pcDNA3.1(+)	T7	BGH	mammalian expression	Ampicillin	Fig. 2
P13	Vinculin-Clover-CC-M2-mRuby2	pcDNA3.1(+)	T7	BGH	mammalian expression	Ampicillin	Fig. S3
2P14	Vinculin-Clover-CC-Mad-mRuby2	pcDNA3.1(+)	T7	BGH	mammalian expression	Ampicillin	Fig. S3
P15	pcDNA3.1-Vh-clover-GCN4-(GGS)3-Vt	pcDNA3.1(+)	T7	BGH	mammalian expression	Ampicillin	S2
P16	pcDNA3.1-Vh-clover-GCN4- GGS)12-Vt	pcDNA3.1(+)	T7	BGH	mammalian expression	Ampicillin	S2
P17	pET28a-AviTag-S0	pET28a	T7F	T7R	bacterial expression	Kanamycin	Fig. 4 & Fig. S9
P18	pET28a-AviTag-S2	pET28a	T7F	T7R	bacterial expression	Kanamycin	Fig. 4& Fig. S9
P19	tCRMod-GGSGGS7	pcDNA3.1(+)	T7F	T7R	mammalian expression	Ampicillin	Fig. 5, Fig. S10

Supplementary figure 1
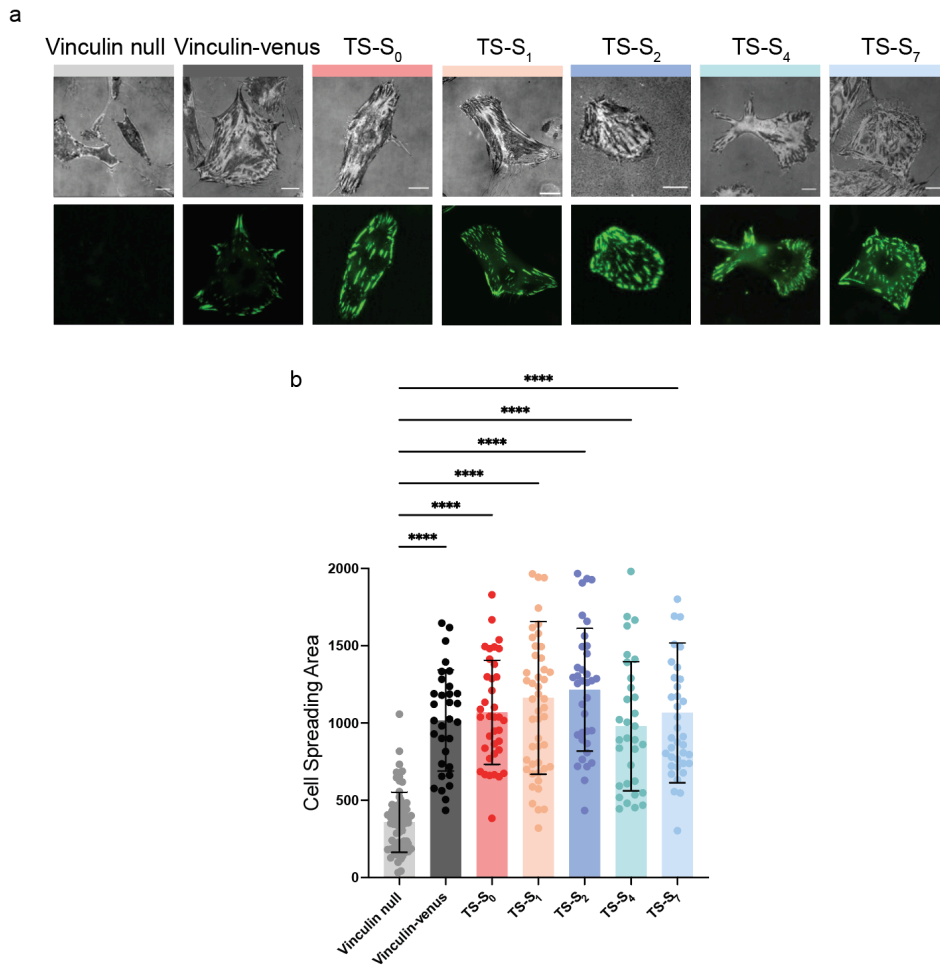
Figure S1: Cell spreading area after transfection with antiparallel CCTS. (a) cell spreading images for vinculin null cells, vinculin-Venus and CCTSs. (b) analysis of spreading area for constructs in (a). **** p <0.0001.

All antiparallel CCTSs used in this study showed same spreading phenotype as vinculin-venus and showed greater spreading area compared to vinculin-null cells (**Figure S1**). The spreading phenotype of Vinculin null cells transfected with CCTS construct are all statistically no difference with vinculin-Venus, having larger spreading area than Vinculin null cells.

Supplementary figure 2
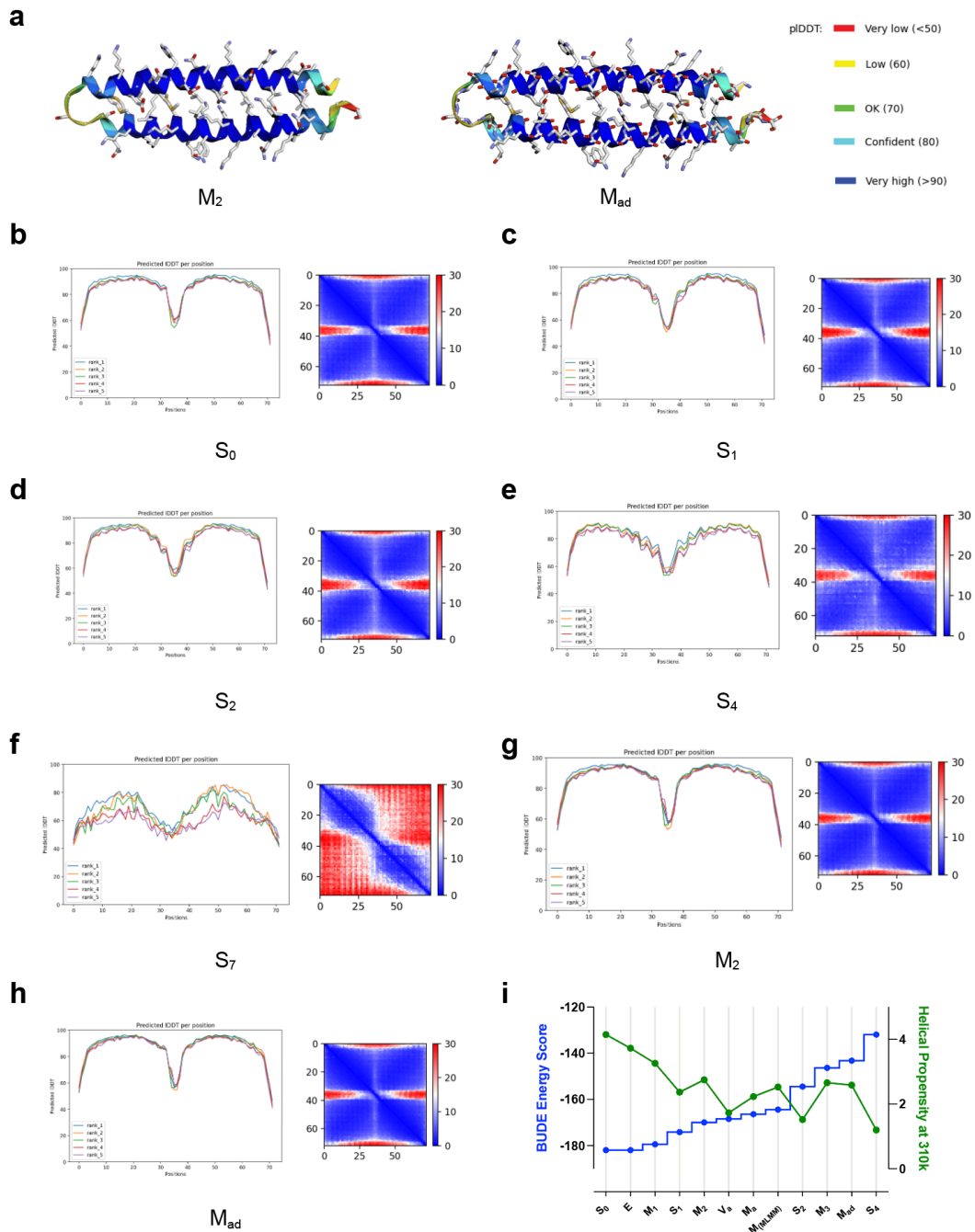
Figure S2. Structure prediction using AlphaFold2 and CCBuilder interaction energy score. (a) Predicted structure generated using AlphaFold2 for CC-M_2 and CC-M_{ad}. Confidence score of the prediction was indicated in the legend to the right. (b-h) Predicted local distance difference test (plDDT) (left) and predicted aligned error (Å) (right) of AlphaFold2 structure analysis for CC-S_0, CC-S_1, CC-S_2, CC-S_4, CC-S_7, CC-M_2, CC-M_{ad}, respectively (n =5). (i) BUDE score and alpha helical propensity of all designed CC library sequences.

Supplementary figure 3
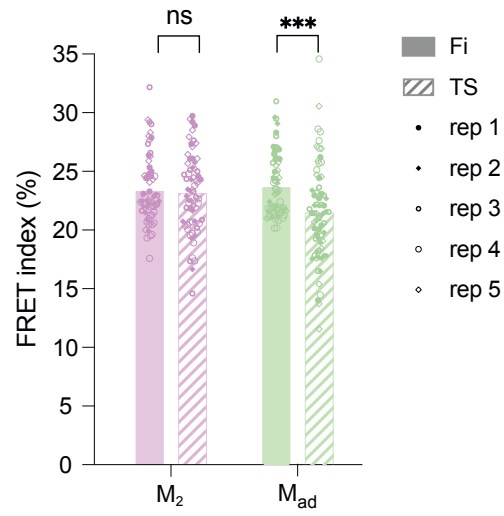
Figure S3. Ensemble FRET measurements in cell experiment for methionine mutations. Quantification of FRET index comparing Fi and TS constructs among the methionine mutations. Each data represents an average FRET index of individual cell (n=63 and 65 for Fi and n =67 and 70 for TS, pooled from five individual experiments). *** p <0.0005, unpaired t-test, two-tailed, assuming equal SD.
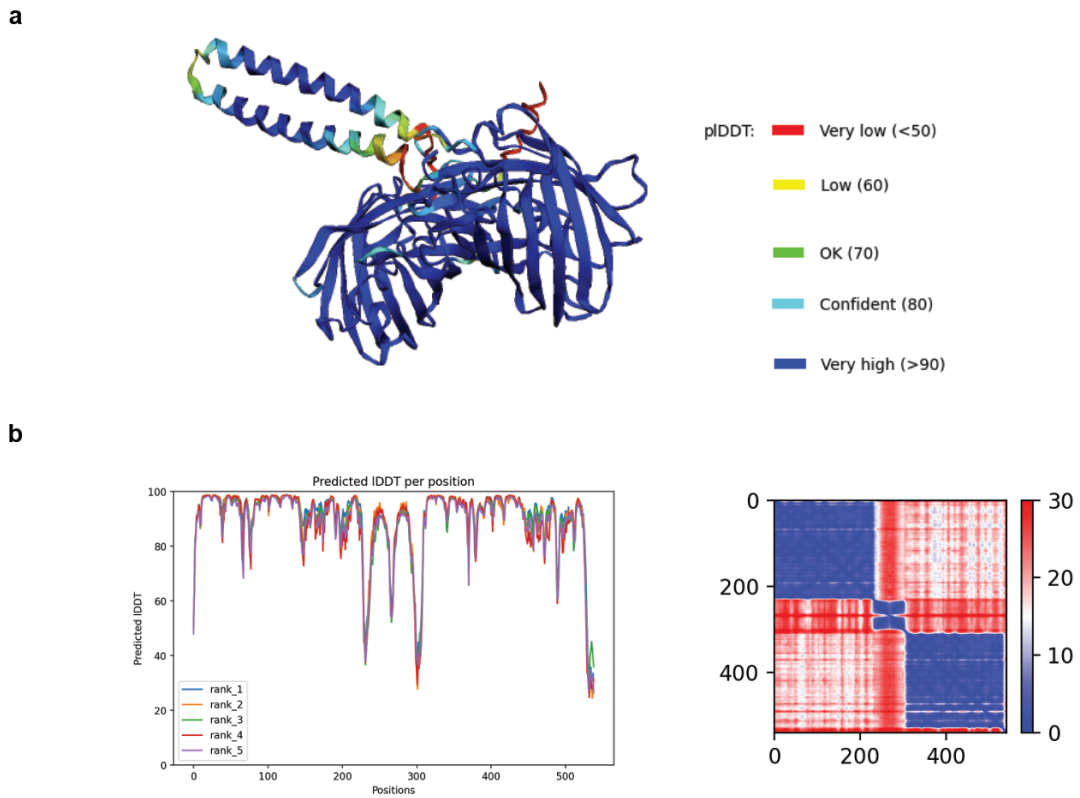
Supplementary figure 4

a

b

Figure S4. AlphaFold2 structural prediction of CCTS with Clover and mRuby2 as FRET pair. (a) 3D rendering of predicted structure generated using AlphaFold2 for Clover-S_0-mRuby2. Confidence score of the prediction was indicated in the legend to the right. (b) plDDT and predicted aligned error of AlphaFold2 structure analysis for Clover-S_0-mRuby2, (n=5).

19
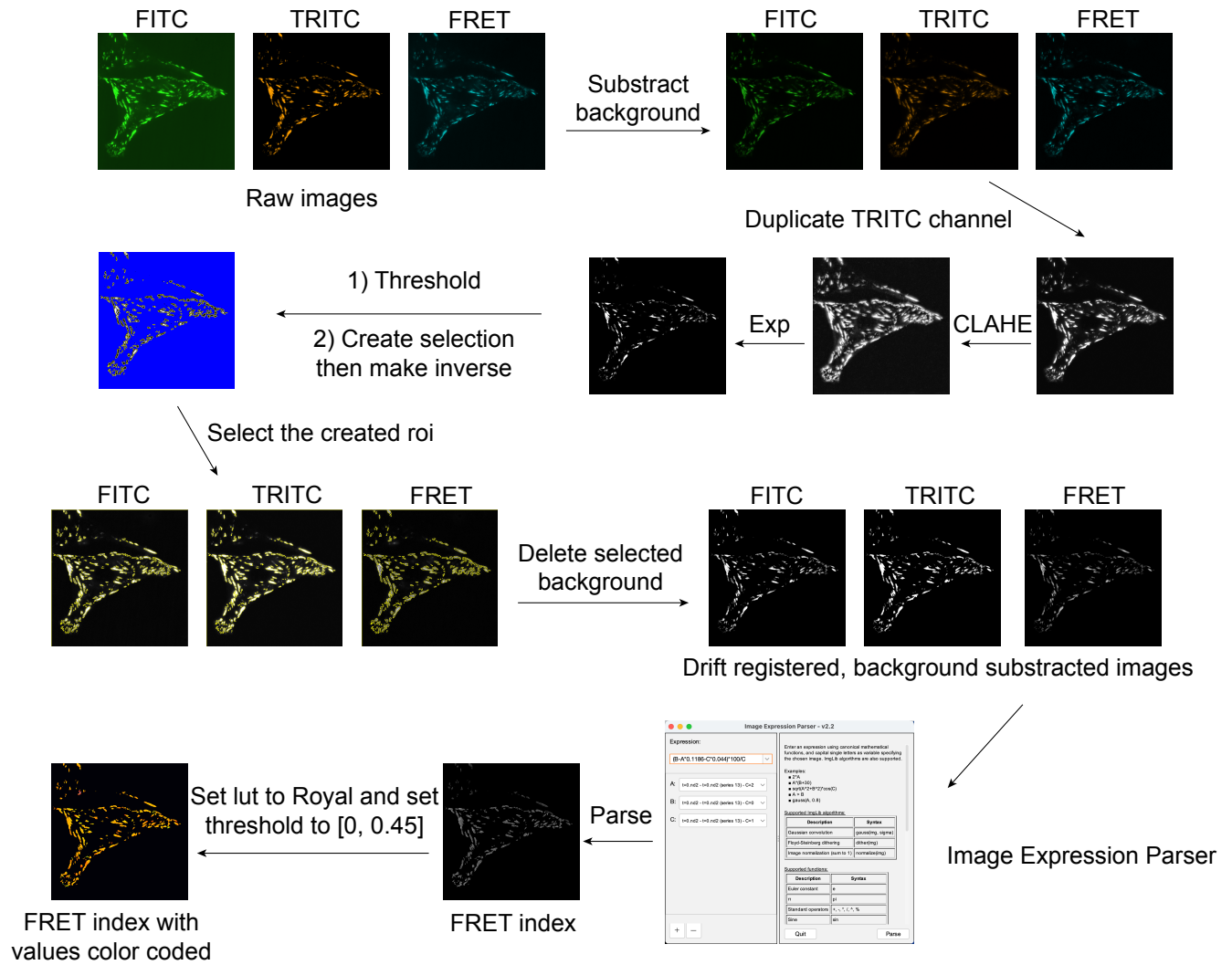
Figure S5. FRET analysis workflow using ImageJ. Scheme of ImageJ FRET index analysis workflow using a cell transfected with Fi-S$_2$ as an example.

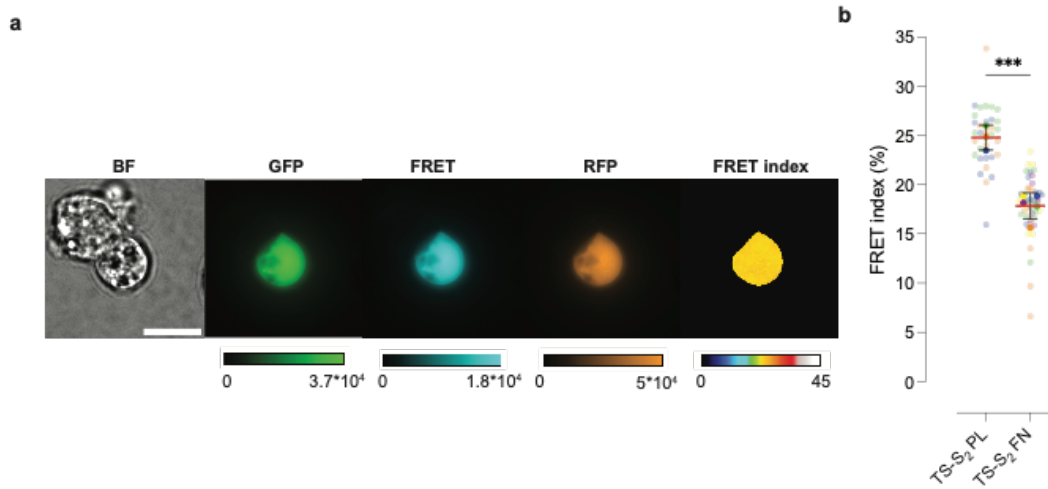**Supplementary figure 6**

Figure S6. Vinculin null cells transfected with TS-S$_2$ seeded on PL coated glass surface display FRET when no adhesion occurs. (a) Vinculin null cells transfected with TS-S$_2$ construct seeded on poly-L-lysine coated glass surface. Images from left to right were taken from bright field, clover channel, FRET channel, mRuby2 channel, respectively 4 hrs after seeding, with FRET index image on the far right. Scale bar =10 μm. (b) TS-S$_2$ PL represents quantification of FRET index of cells in the condition described in (a). Each data represents an average FRET index of individual cell. Data points with each color represent cells from each individual pool (n=11, 10, 12 pooled from three individual experiments). Mean =25%; stand deviation of the mean =1.3%. TS-S$_2$ FN data is pooled from **Figure 2b** TS-S$_2$ for comparison.
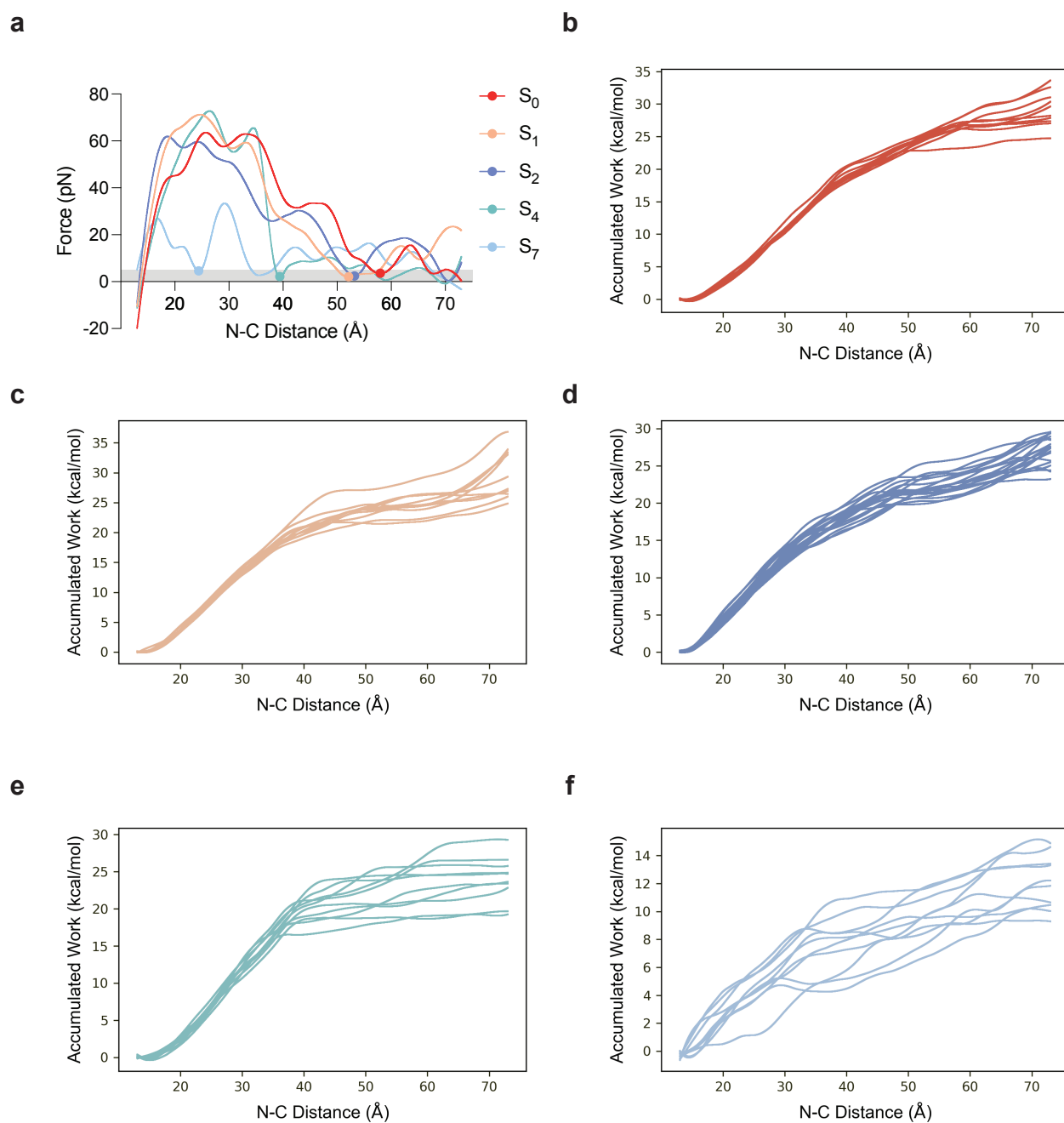
Supplementary figure 7

Figure S7. Force-Distance curve from first derivative of accumulated work in SMD data and replicates for each CC. (a) First derivative of accumulated work from plot in figure 3d. Note that each filled circle indicates the N-C distance position associated with minimum energy in the simulation. (b-f) SMD simulation replicates for S_0, S_1, S_2, S_4, S_7, respectively.

Table S3. N-C distance and accumulated work value at lowest force for serine CC mutants.

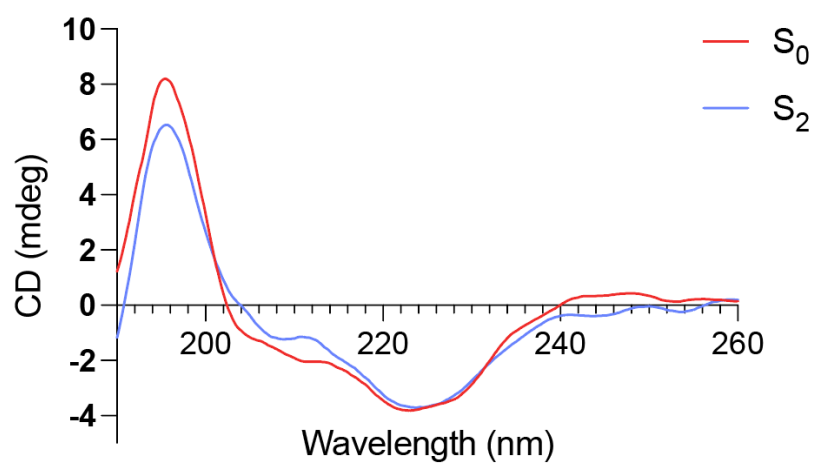|	N-C Distance (Å)	Total work to unfold the CC (kcal/mol)	Force (pN)
S_0	24.44	24.54	3.46
S_1	39.41	22.62	2.00
S_2	53.19	21.33	2.27
S_4	52.12	17.80	2.05
S_7	57.97	2.47	4.46

Supplementary figure 8

Figure S8. Circular dichroism of CCs. Circular dichroism of expressed CC-S_0 (red line) and CC-S_2 (blue line). Circular dichroism for CC-S_0 or CC-S_2 both showed alpha helical structure, which indicates that the protein maintains its secondary structure after bacterial expression.
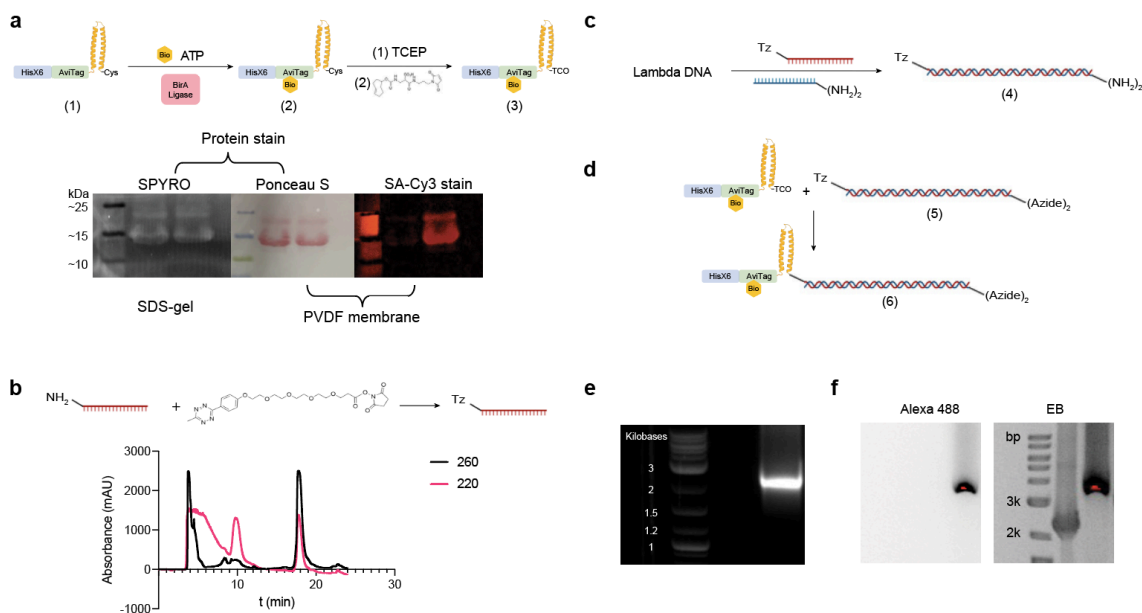
Supplementary figure 9

Figure S9. CC-DNA conjugation for optical trap measurements. Procedure for CC-DNA conjugation. (a) CC fused with HisTag and Avitag (1) was expressed from bacteria (E. coli), then biotinylated (2) and reduced by immobilized TCEP resins and reacted with TCO-maleimide to form product (3). Western blot shows two lanes for 1(left) and 2(right). The protein stains, SPYRO and Ponceau S confirm the presence of 1 and 2. The streptavidin-Cy3 (SA-Cy3) staining signal on far right confirms that 2 is biotinylated in contrast to the starting material 1 lacking biotin. (b) Forward primer (red) has a 5' amine modification and was reacted with NHS-(peg)$_4$-tetrazine. HPLC purified product was collected at about 18 min as shown in chromatogram. (c) DNA handle was synthesized through PCR with tetrazine modified forward primer (red) and a bis-amine modified reverse primer (blue) and a lambda DNA template. The amines were subsequently coupled with NHS-azide to generate (5). (d) CC-TCO (3) was reacted with tetrazine-DNA handle (5) to create CC-DNA conjugate (6). (e) Agarose gel after PCR. The gel shows production of product 4 with 2.3 kbases. (f) SDS-page gel in Alexa 488 channel and Ethidium bromide channel.

The CC-S$_0$ and CC-S$_2$ were fused with HisTag for purification and AviTag for biotinylation at the N terminus with a C terminus cystine for chemical modification. These constructs were expressed using BL21-CodonPlus(DE3)-RIPL *E. coli* (Agilent) then purified using Ni-NTA column to obtain molecule (1). Then BirA ligation on molecule (1) covalently tagged biotin to a lysine residue within the AviTag at the N-terminus of the peptide. Biotinylation was confirmed using western blot with SA-Cy3 staining (**Figure S9a**). Then the biotinylated protein (2) was reduced using immobilized TCEP resins to avoid oligomerization via terminal cysteines and then reacted with TCO-maleimide to introduce TCO to the terminal cysteine residue (3). 5'-amine modified forward primer was reacted with NHS-(peg)4-tetrazine to introduce tetrazine (Tz) groups to the primer (**Figure S9b**). Product (with both DNA (black line) and Tz (red line) absorbance) was collected via HPLC at about 18 min. Reverse primer included 5'-bis-amine group. To create the DNA handle (4), we conducted PCR using lambda DNA as a template (**Figure S9c**). Because the Tz group is stable in the thermal cycling needed for PCR but not the azide group, we functionalized the forward primer with Tz before PCR and functionalized the DNA handle with azide after PCR. The DNA handle (4) was then reacted with Azide-(peg)4-NHS (DMSO) to introduce a bis-azide group (5). Then the DNA handle (5) was conjugated to the C-terminus of TCO modified CC protein (3) via a Tz-TCO click reaction to create molecule (6) (**Figure S9d**). DNA size after PCR was confirmed using agarose gel with a band at slightly above 2k bp (**Figure S9e**). The reaction in **Figure S9d** was desalted and reacted with NHS-alexa488 to tag the protein with a fluorescence signal. Molecule (5) and purified reaction in **Figure S9d** were loaded to an agarose gel and stained with ethidium bromide (EB). Molecule (5) showed only EB signal but not 488 signal as expected, while reacted product showed both 488 and EB signal as well as a mobility shift which indicates the success of Tz-TCO conjugation (**Figure S9f**).
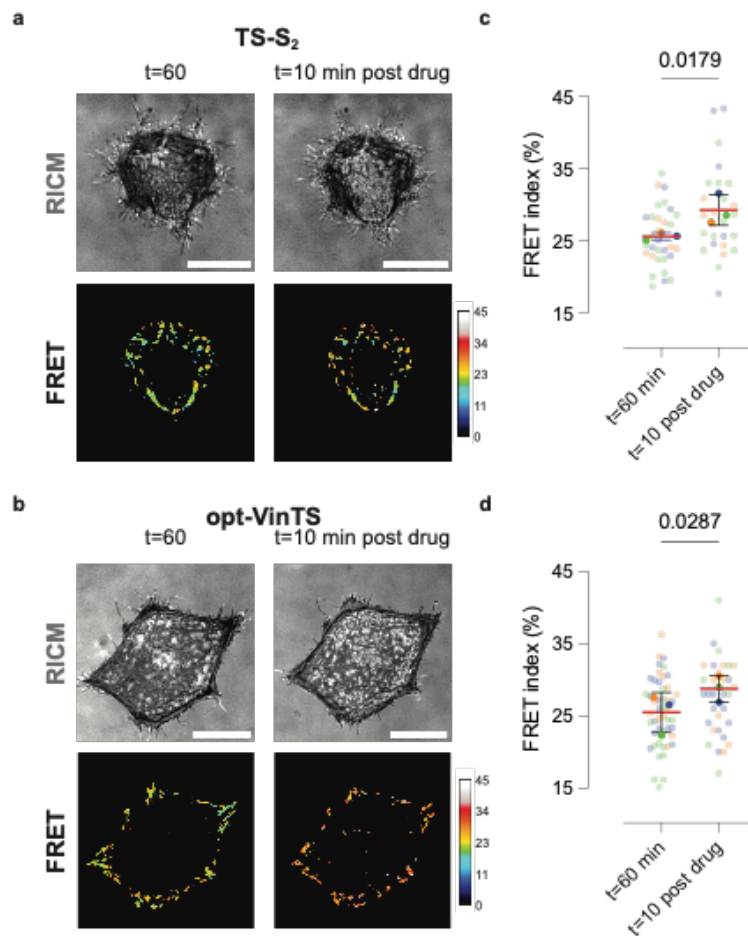
Supplementary figure 10

Figure S10. Latrunculin B treatment on vinculin null cells transfected with TS-S$_2$ and opt-VTS. **(**a,b) Representative RICM images (top) and FRET index images (bottom) of vinculin null cells transfected with (a) TS-S$_2$ and (b) opt-VinTS construct after seeded on fibronectin coated glass surface 60 min and 10 min after adding latrunculin B to the cell at t =60 min. (c,d) Quantification of FRET index comparing cells at t =60 min and after 10 min latrunculin B incubation of cells ar 60 min for (c) TS-S$_2$ and (d) opt-VinTS. Each data represents an average FRET index of individual cell. Data points with each color represent cells from each individual pool from three experiments (n >30). p values shown on top of compared columns in the figure, unpaired t-test, two-tailed, assuming unequal SD.

SUPPORTING INFORMATION

Movie S1: Spin Movie of Clover-S_0-mRuby2 3D rendering structure predicted by AlphaFold2.

Movie S2: An example of SMD simulation of CC-S_0 unfolding dynamics.

SUPPORTING INFORMATION

References

[1]   A. S. LaCroix, A. D. Lynch, M. E. Berginski, B. D. Hoffman, *eLife* **2018**, *7*, e33927.
[2]   C. Grashoff, B. D. Hoffman, M. D. Brenner, R. Zhou, M. Parsons, M. T. Yang, M. A. McLean, S. G. Sligar, C. S. Chen, T. Ha, M. A. Schwartz, *Nature* **2010**, *466*, 263-266.
[3]   S. K. Vester, R. Rahikainen, I. N. A. Khairil Anuar, R. A. Hills, T. K. Tan, M. Howarth, *Nat Commun* **2022**, *13*, 3714.
[4]   R. Sharma, S. Narum, S. Liu, Y. Dong, K. I. Baek, H. Jo, K. Salaita, *ACS Chemical Biology* **2023**, *18*, 2349-2367.
[5]   J. C. Phillips, R. Braun, W. Wang, J. Gumbart, E. Tajkhorshid, E. Villa, C. Chipot, R. D. Skeel, L. Kalé, K. Schulten, *Journal of Computational Chemistry* **2005**, *26*, 1781-1802.
[6]   J. Huang, S. Rauscher, G. Nawrocki, T. Ran, M. Feig, B. L. de Groot, H. Grubmüller, A. D. MacKerell, *Nature Methods* **2017**, *14*, 71-73.
[7]   W. L. Jorgensen, J. Chandrasekhar, J. D. Madura, R. W. Impey, M. L. Klein, *The Journal of Chemical Physics* **1983**, *79*, 926-935.
[8]   G. J. Martyna, D. J. Tobias, M. L. Klein, *The Journal of Chemical Physics* **1994**, *101*, 4177-4189.
[9]   T. Darden, D. York, L. Pedersen, *The Journal of Chemical Physics* **1993**, *98*, 10089-10092.
[10]   H. Chen, D. M. Cohen, D. M. Choudhury, N. Kioka, S. W. Craig, *J Cell Biol* **2005**, *169*, 459-70.
[11]   A. J. Lam, F. St-Pierre, Y. Gong, J. D. Marshall, P. J. Cranfill, M. A. Baird, M. R. McKeown, J. Wiedenmann, M. W. Davidson, M. J. Schnitzer, R. Y. Tsien, M. Z. Lin, *Nat Methods* **2012**, *9*, 1005-12.
[12]   T. J. Lambert, *Nature Methods* **2019**, *16*, 277-278.
[13]   P. Ringer, A. Weissl, A. L. Cost, A. Freikamp, B. Sabass, A. Mehlich, M. Tramier, M. Rief, C. Grashoff, *Nat Methods* **2017**, *14*, 1090-1096.
[14]   C. Grashoff, B. D. Hoffman, M. D. Brenner, R. Zhou, M. Parsons, M. T. Yang, M. A. McLean, S. G. Sligar, C. S. Chen, T. Ha, M. A. Schwartz, *Nature* **2010**, *466*, 263-6.
[15]   Y. Ren, Yang, J., Jin, H., Zhang, Y., & Berro, J.. , **2021**.
[16]   Y. Ren, J. Yang, B. Fujita, H. Jin, Y. Zhang, J. Berro, *Science Advances* **2023**, *9*, eadi1535.
[17]   M. Goktas, C. Luo, R. M. A. Sullan, A. E. Bergues-Pupo, R. Lipowsky, A. Vila Verde, K. G. Blank, *Chemical Science* **2018**, *9*, 4610-4621.
[18]   C. Jarzynski, *Physical Review Letters* **1997**, *78*, 2690-2693.
[19]   R. Killick, P. Fearnhead, I. A. Eckley, *Journal of the American Statistical Association* **2012**, *107*, 1590-1598.
[20]   B. Andreopoulos, D. Labudde, *Algorithms for Molecular Biology* **2011**, *6*, 16.
[21]   S. Buck, L. Pekarek, N. Caliskan, *Biophysical Journal* **2022**, *121*, 2830-2839.
[22]   T. Odijk, *Macromolecules* **1995**, *28*, 7016-7018.
[23]   M. D. Wang, H. Yin, R. Landick, J. Gelles, S. M. Block, *Biophys J* **1997**, *72*, 1335-46.